Confinement-Induced Transition between Wavelike Collective Cell Migration Modes

Vanni Petrolli,[1] Magali Le Goff,[1] Monika Tadrous,[1,*] Kirsten Martens,[1] Cédric Allier,[2] Ondrej Mandula,[2] Lionel Hervé,[2] Silke Henkes,[3] Rastko Sknepnek,[4,5] Thomas Boudou,[1] Giovanni Cappello,[1,†] and Martial Balland[1,‡]

[1]*Université Grenoble Alpes, Laboratoire Interdisciplinaire de Physique, CNRS, F-38000 Grenoble, France*
[2]*CEA, LETI, MINATEC, 17 rue des Martyrs, 38054 Grenoble cedex 9, France*
[3]*Department of Mathematics, University of Bristol, Bristol BS81TW, United Kingdom*
[4]*School of Science and Engineering, University of Dundee, Dundee DD1 4HN, United Kingdom*
[5]*School of Life Sciences, University of Dundee, Dundee DD1 5EH, United Kingdom*

(Received 17 December 2018; published 24 April 2019)

The structural and functional organization of biological tissues relies on the intricate interplay between chemical and mechanical signaling. Whereas the role of constant and transient mechanical perturbations is generally accepted, several studies recently highlighted the existence of long-range mechanical excitations (i.e., waves) at the supracellular level. Here, we confine epithelial cell monolayers to quasi-one-dimensional geometries, to force the establishment of tissue-level waves of well-defined wavelength and period. Numerical simulations based on a self-propelled Voronoi model reproduce the observed waves and exhibit a phase transition between a global and a multinodal wave, controlled by the confinement size. We confirm experimentally the existence of such a phase transition, and show that wavelength and period are independent of the confinement length. Together, these results demonstrate the intrinsic origin of tissue oscillations, which could provide cells with a mechanism to accurately measure distances at the supracellular level.

DOI: 10.1103/PhysRevLett.122.168101

Supracellular organization plays a key role in establishing and maintaining structure, function, and homeostasis in tissues. In the early stages of embryonic development, where features need to arise spontaneously from a homogeneous state, this organization closely follows morphogenic chemical patterns. In the most general case, however, chemical reactions, osmotic pressures and mechanical forces all cooperate to determine tissue-level organization. This is confirmed by an increasing number of recent studies indicating that cell proliferation, differentiation, and motility are strongly impacted by the mechanical properties of the microenvironment [1–5]. Several recent works reported that wavelike patterns of the local cell velocity spontaneously appear in colonies of epithelial cells. Those velocity waves have also been observed in spreading epithelial sheets [6–9], regardless of cell proliferation [10], and are correlated to oscillations of the forces exerted by the cells on the substrate [11]. Such long wavelength patterns also appear in confined geometries where cell migration is limited to local cell rearrangements [12–16]. These waves are characterized by a wavelength λ and a period T, and show a surprisingly large spatial and temporal coherence. They can be modeled either at the particle level [15] or using continuum approaches [10,16], based on a coupling between cell motility and intercellular forces.

In this Letter, we explore whether the period and wavelength of collective wave excitation in epithelial cell monolayers are intrinsically encoded in the activity of the cell, or if they are affected by external constraints such as a specific set of boundary conditions. To achieve this, we analyzed the collective motion of epithelial cells confined to a quasi-one-dimensional channel. The experiments were accompanied by a series of numerical simulations, based on a self-propelled Voronoi model (SPV) [17–19], adapted to take into account the confining geometry. Our results show that tuning the length of the confining channel drives a phase transition between a state of global oscillations and a multinodal wave state. This transition is a consequence of the interplay between local cell active dynamics and global confinement. The effect is robust and does not require detailed knowledge of molecular processes but relies on a simple polarity-velocity alignment mechanism studied in the physics of dense active matter systems.

To confine cells to a quasi one-dimensional pattern, we prepared adherent stripes on soft polyacrylamide gels ($E \simeq 40$ kPa), as described previously [20] [outlined in Fig. 1(a)]. Stripes of different length ($L_X = 100$ to 2000 μm), but of the same width ($L_Y = 40$ μm), were patterned on the same substrate. Epithelial Madin-Darby Canine Kidney (MDCK) cells were then seeded on the patterned substrates with initial concentration of $2.5 \pm 0.5 \times 10^4$ cells/cm^2. The samples were washed with fresh medium 1 h after seeding, then placed in the incubator (37 °C and 5% CO_2) until the end of the experiments. Cells were imaged *in situ* using an in-line holographic (defocus) microscope (see and Fig. SI-1 and Supplemental Material [21],

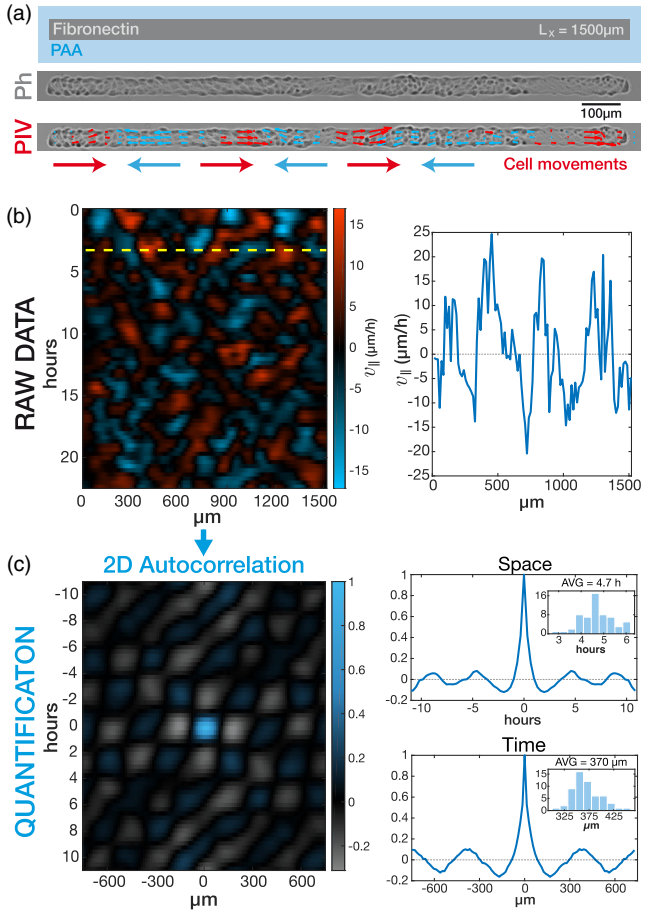

FIG. 1. (a) Top: MDCK cells are seeded onto a polyacrylamide (PA) gel patterned with fibronectin stripes (width: $L_Y = 40$ μm, length: $L_X = 1500$ μm). Middle: phase-contrast image of a confluent tissue. Bottom: velocity field measured by PIV. Velocities pointing in the positive (negative) x-axis direction are shown in red (blue), in agreement with the arrows reported under the image. (b) Left: kymograph representing the average horizontal velocity $v_{\parallel}(x;t)$ in time. Right: an example of velocity profile along the dashed line. We removed low frequency drifts using a Gaussian high-pass filter. (c) To quantify the periodicity of oscillations, we calculate the spatiotemporal autocorrelation of the kymograph (left) and measure peak spacing along the spatial (top-right) and temporal (bottom-right) coordinates (insets: distribution of peak periodicity for $n = 59$ independent stripes). Images in panels (b), (left) and (c), (left) were smoothed for visualization purposes with a low-pass Gaussian filter ($\sigma_x = 15$ μm, $\sigma_t = 30$ min).

which includes Refs. [22,23]) [24] for ≃48 h after confluence, gathering one image every 10 min [e.g., Fig. 1(a), middle]. Cell velocities were computed with a custom-made particle image velocimetry (PIV) algorithm with a final resolution of 20 min and 14 μm. To generate the kymograph, we cropped the videos in time to consider only confluent tissues, in an interval where the average absolute velocity was higher than 4 $\mu m/h$ [25]. We then averaged the horizontal component of the speed along the transverse direction $v_{\parallel}(x;t) = \langle v_x(x,y;t)\rangle_y$. We removed low frequency drifts using a Gaussian high-pass filter cropping 50% of the signal at 700 μm and 10 h. The kymograph in Fig. 1(b), left represents the spatiotemporal evolution of the velocity field over 22 h and over the whole stripe. A typical instantaneous velocity profile [Fig. 1(c), right] displays periodic oscillations in space. To quantify the period and the wavelength of these oscillations, we computed the autocorrelation function of the kymograph $g(\delta x,\delta t) = \langle v_{\parallel}(x,t)v_{\parallel}(x+\delta x,t+\delta t)\rangle_{x,t}$, displayed in Fig. 1(c), left. We observe an oscillating pattern in the autocorrelation function, both along the spatial and the temporal directions [Fig. 1(c), right]. This pattern indicates the establishment of an extended multinodal standing wave, with wavelength and period equal to $\lambda = 370 \pm 30$ μm and $T = 4.7 \pm 0.7$ h, respectively (errors represent the standard deviation, $n = 59$) [see histograms in Fig. 1(c), right].

To obtain a detailed understanding of oscillations in tissues, we consider a computational framework based on a recently introduced self-propelled Voronoi model [17–19]. The model used in this study is similar to that used in Ref. [19] to describe flocking transitions in confluent tissues, but rather than using periodic boundary conditions, we imposed confinement through a repulsive rectangular wall of size (L_X, L_Y) to reproduce the experiments' geometry. Full details of the model and its implementation can be found in Ref. [18] (also see Supplemental Material [21] for the parameters used). Briefly, the confluent cell monolayer is modeled as a two-dimensional network of Voronoi polygons covering the plane [Voronoi tessellation of all cell center positions, see Fig. 2(a)]. Each configuration of cells is described by the positions of cell centroids with energy given by the commonly used Vertex model [26], which depends on the area and perimeter of each cell. The parameters of the Vertex model include area and perimeter stiffness constants (K and Γ) and target area and perimeter (A^0 and P^0). These parameters were chosen to describe a monolayer in a solidlike regime (with a shape factor $p^0 = P^0/\sqrt{A^0} = 2.5$) [17,27], to avoid shear flows induced by the boundaries. As in Refs. [17–19], we consider an overdamped dynamics, i.e., a force balance between frictional force with the substrate, self-propulsion at a constant velocity v_0 along the direction of cell polarity $\mathbf{n}_i$, and mechanical forces between the cells determined as a negative gradient with respect to cell position of the SPV model energy functional. The value of v_0 can be set to match the experimental observations, but does not affect the general oscillatory behavior. The dynamics of the cell polarity $\mathbf{n}_i$, described by the angle θ_i with the x axis of the laboratory reference frame [i.e., $\mathbf{n}_i = (\cos(\theta_i), \sin(\theta_i))$] are

$$\frac{\partial \theta_i}{\partial t} = \frac{1}{\tau_{al}} \sin(\theta_i - \phi_i) + \nu_i^r(t), \tag{1}$$

with ϕ_i being the angle between the velocity of cell i and the x axis, and $\nu_i^r(t)$ being an orientational Gaussian noise. The angular dynamics is thus controlled by the interplay of

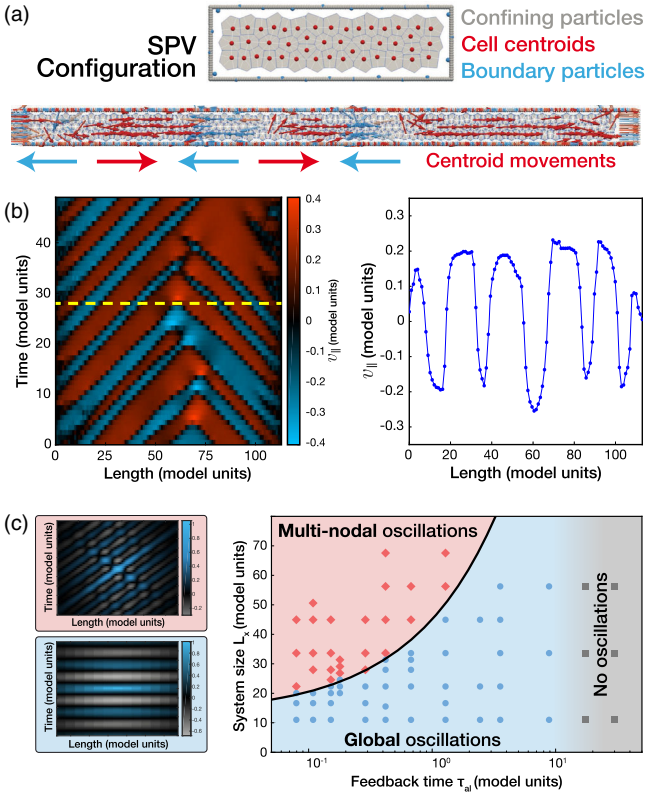

FIG. 2. Self-propelled Voronoi model for collective oscillations in confluent tissues.(a) Top: Example of tissue configuration obtained from the integration of the SPV model. Voronoi tessellation of the plane and centroid positions. Bottom: Velocity field of the centroids of the tesselation. Velocities pointing to the positive direction on the x axis are represented in red and to the negative direction in blue. (b) Left: Kymograph representing the average horizontal velocity $[v_{\parallel}(x;t)]$ over time and right: its profile along the dotted line. (c) Phase diagram of oscillation patterns in the SPV model in the $(\tau_{al} - L_X)$ plane. Two types of oscillations are observed depending upon the system size $L_X(\tau_{al})$: Top left: For large systems where $L_X > L_X^c(\tau_{al})$ the autocorrelation of the kymograph shows multinodal oscillations whereas for small systems (bottom, left) where $L_X < L_X^c(\tau_{al})$ the autocorrelation exhibits global oscillations. Right: Simulation data points indicating whether the system exhibits global (blue disks), multinodal (red diamond), or no oscillations (gray squares symbols) for large values of the feedback timescale ($\tau_{al} > \tau_{al}^c \approx 17$ model time units). The solid line delimiting the global and multinodal oscillation phases is a power-law fit of the transition data points [$L_X^c(\tau_{al}) = a\tau_{al}^b + c$ with $a \simeq 32$, $b \simeq 0.62$, $c \simeq 13$].

rotational diffusion (kept constant in this study) and the polarity-velocity alignment with rate τ_{al}^{-1}, with τ_{al} being the time required by the cell to reorient its polarization in the direction of its velocity. This feedback mechanism leads to oscillations in confinement, where τ_{al} plays the role of an effective inertia, and the oscillations are along the lowest-energy elastic modes of the material [28]. This feedback mechanism is also at the origin of flocks in nonconfined tissues [19]. Simulations of confined tissue layers show steady state oscillations akin to those observed in experiments [Fig. 2(a), bottom]. In the following, we study the dependence of these oscillations on the confining length L_X and show that a feedback mechanism for alignment (through τ_{al}) is key to observe such mechanical waves in the SPV model. First we consider the case of long confining channels, where multinodal oscillations were observed experimentally [Fig. 1]. The simulation results displayed in Fig. 2(b) are obtained for a system with the same transverse confining length L_Y (about 3 cells in the y direction) and aspect ratio as in the experiments in Fig. 1 (and a value $\tau_{al} = 0.3$). We observe a pattern in the x component of the velocity $v_{\parallel}$, and using the same analysis tools as in Fig. 1, we extract the wavelength $\lambda_{\mathrm{SPV}} \approx 22$ model length units and the period $T_{\mathrm{SPV}} \approx 8$ model time units. Note that by approximately matching the timescale of the model to the experiments (through the cells velocity v_0), one would get from these simulation data $\lambda \approx 300$ μm and for the period $T \approx 2$ h. This indicates that this model is able to reproduce the features observed in the experiments, although some fine-tuning of parameters (τ_{al}, v_0) is required for a quantitative match. Note that although the instantaneous velocity profiles [Fig. 2(b), right] and autocorrelation [Fig. 2(c), top left] plots appear to be similar to the experiments, the full spatiotemporal dynamics of the model [Fig. 2(b), left] do not correspond to standing wave oscillations. If the system size L_X is decreased (keeping the value of τ_{al} constant), the number of nodes also decreases down to a point where the system size can only accommodate a single spatial period of oscillation, reaching a regime of global oscillation, where the direction of motion of all cells is coordinated [Fig. 2(c), top left]. This transition, illustrated in Fig SI-3 [21], is shown in the $\tau_{al} - L_X$ plane in Fig. 2(c), right. The feedback timescale also plays an important role as no oscillations are observed if τ_{al} is too large (i.e., the noise dominates over the coupling), and the critical length L_X^c at which one observes multinodal oscillations increases with τ_{al}. In the small system regime, the oscillation period increases linearly with the system size, as previously reported [15,16], and with τ_{al} (until oscillations eventually vanish for large values of τ_{al}), consistent with the role of the feedback mechanism as an effective inertia [28]. Therefore, the SPV model describes a transition controlled by the stripe length $L_X^c(\tau_{al})$ between global oscillations where all cells coordinate their motion to a regime where groups of cells coordinate their motion direction locally.

To verify this prediction, we varied the length L_X of the stripe between 100 and 2000 μm (examples between 200 and 1000 μm in Fig. 3), in order to tune the system across the critical length L_X^c. In approximately 95% of experiments, in agreement with model predictions, we observed two types of behaviors: (i) A global movement of all cells alternating between rightward and leftward motion [as seen

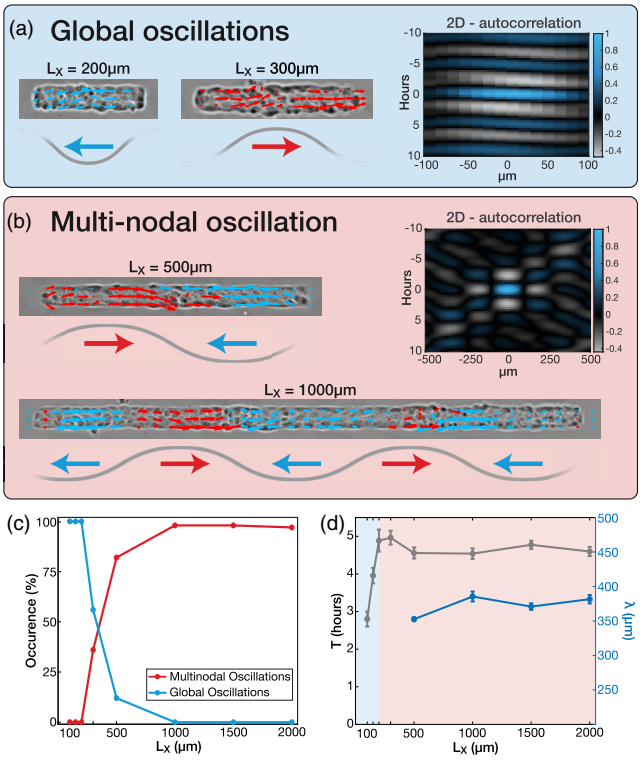

FIG. 3. Dependence of oscillatory behavior on the stripe length. (a) The velocity field superimposed on phase contrast images for short stripes of length 200 and 300 μm displays global oscillations, generating a characteristic two-dimensional autocorrelation (right). Longer lines (500 and 1000 μm) display multinodal oscillations (b), which give rise to a different pattern in the autocorrelation image (right). Velocities pointing in the positive x-axis direction are represented in blue, those pointing in the negative x-axis direction are represented in red, in agreement with the arrows reported in the schemes under each image. For each length, we display the frequency of each phenotype (c) and the characteristic time and space periodicity (d) calculated. Bars represent the standard error of the mean.

from the autocorrelation function of the kymograph in Fig. 3(a)] and (ii) the establishment of a multinodal standing wave with antinodal cells moving back and forth and cells at the nodes being alternately compressed and dilated [Fig. 3(b)]. The incidence of the two behaviors strongly depends on L_X, with a transition for $L_X \simeq \lambda$. In the experiments with $L_X < 200$ μm, the global oscillation statistically dominated. In this case, the period scales linearly with the tissue size [Fig. 3(d), blue area], while the wavelength is imposed by the confinement. In large structures ($L_X > 500$ μm), we only found multinodal waves, with the period and wavelength independent of L_X [Fig. 3d, red area]. Figure 3(c) quantifies the transition, with on average 39 tissues per point, obtained from three independent experiments. Our experiments confirmed the existence of a self-sustained oscillatory mode in epithelial layers. Using the typical period and wavelength, we can define an effective velocity $u_\phi = L_X/T \simeq 78 \pm 13$ μm/h, which is independent of the pattern size. Even for small patterns ($L_X < 500$ μm), this velocity is preserved as the period scales linearly with the pattern length. We also note that u_ϕ is approximately tenfold larger than the average speed of individual cells within the epithelial layer (between 4 and 12 μm/h, depending on cell density [25,29]). Eventually, the spatial coherence of supracellular waves exceeds the largest pattern observable with our microscope.

Simulations using the SPV model show the emergence of sustained collective oscillations in confined monolayers. We identified two crucial conditions to produce these oscillations: (i) The existence of a delayed feedback between cell velocity and self-propulsion direction to introduce a new timescale in the dynamics and (ii) a very limited number of cellular rearrangement, at the limit of the solidlike regime. These ingredients allow the system to be described by linear elasticity, and for oscillations along the lowest energy elastic modes to dominate the dynamics [28]. One could thus envision tuning the oscillations by controlling cell-cell interactions through RAB5 or cadherin-mediated junctions, without affecting cells' individual mobility [19,30]. Contrary to experiments, where multinodal standing waves are observed, the SPV model describes propagating oscillations. Several reasons may explain this difference. First, a standing wave is only established when the wavelength exactly matches the boundary conditions. Thus, models require fine-tuning of the pattern length, while the intrinsic variability between cells could make the real epithelium more adaptable to small variations of the confinement size. Second, a different choice of the coupling mechanism could also introduce a new timescale in the model and better describe standing waves in confined tissue. Two-dimensional SPV models are usually adapted to describe spatially extended monolayers, while the stringent confinement used experimentally makes the system quasi-one-dimensional and induces strong constraints on the shape of cells near the boundary. Such boundary effects are difficult to capture in the SPV model due to the constraint of maintaining a Delaunay triangulation (dual of the Voronoi tesselation) [18], but do not seem to be essential to account for the oscillatory dynamics observed experimentally. One could thus consider building a one-dimensional continuum model based on an elastic description of the monolayer [28] in order to predict the transition between the different oscillatory regimes observed experimentally.

In conclusion, we demonstrate that the typical period and wavelength of epithelial tissue oscillations are intrinsically encoded in the cells, and are not adapted to external confinements. For this system, our SPV model predicts a transition between global oscillation and multinodal waves, the existence of which is confirmed experimentally for a pattern length $L_X^c \simeq 400$ μm. From a biological perspective this transition could be significant. If in small systems all the cells behave similarly—the entire layer alternately moves back and forth—in large systems cells located either at the nodes or at the antinodes experience different

mechanical stimuli and may undergo different fates, which can ultimately lead to supracellular patterning. The existence of an intrinsic wavelength λ also provides an intrinsic metric, likely encoded in the cell. It is interesting to note that λ roughly corresponds to the typical size of a Drosophila embryo (both length and circumference approach 400–500 μm, while cell size is $\simeq$15 μm), the most studied model system for morphogenesis. Based on this consideration, two important biological questions arise. Is this intrinsic metric used by the organism to measure distance inside a developing embryo? Does a collective long range excitation allow cells to probe their distant environment, in a timescale much shorter that allowed by their own motility?

The authors would like to acknowledge I. Wang for the development of Particle Image Velocimetry and P. Moreau for his technical support. We also thank K. Hennig, T. Andersen, E. Vitiello, and C. Guilluy for valuable and supportive discussions. G. C. has been supported by the Institut National de la Santé et de la Recherche Médicale (Grant "Physique et Cancer" PC201407). T. B. and M. B. acknowledge financial support from the CNRS "Mission pour l'Interdisciplinarité" and the Center of Excellence of Multifunctional Architectured Materials "CEMAM" (n AN-10-LABX-44-01). M. B. acknowledges financial support from the ANR MechanoSwitch project, Grant No. ANR-17-CE30-0032-01 of the French Agence Nationale de la Recherche. R. S. and S. H. the UK BBSRC, Grants No. BB/N009789/1 and No. BB/N009150/1-2. M. T. acknowledges iREU NSF Grant No. 1560390 and LSAMP NSF Grant No. 1302873.

*Present address: Mechanical Engineering Department, California State University, Fullerton, CA 92831, USA.
†Giovanni.Cappello@univ-grenoble-alpes.fr
‡Martial.Balland@univ-grenoble-alpes.fr

[1] A. J. Engler, S. Sen, H. L. Sweeney, and D. E. Discher, Cell **126**, 677 (2006).
[2] B. Trappmann, J. E. Gautrot, J. T. Connelly, D. G. T. Strange, Y. Li, M. L. Oyen, M. A. Cohen Stuart, H. Boehm, B. Li, V. Vogel, J. P. Spatz, F. M. Watt, and W. T. Huck, Nat. Mater. **11**, 642 (2012).
[3] G. Helmlinger, P. A. Netti, H. C. Lichtenbeld, R. J. Melder, and R. K. Jain, Nat. Biotechnol. **15**, 778 (1997).
[4] M.-E. Fernandez-Sanchez, F. Serman, P. Ahmadi, and E. Farge, Methods Cell Biol. **98**, 295 (2010).
[5] C.-M. Lo, H.-B. Wang, M. Dembo, and Y.-l. Wang, Biophys. J. **79**, 144 (2000).
[6] B. Ladoux and R.-M. Mège, Nat. Rev. Mol. Cell Biol. **18**, 743 (2017).
[7] V. Hakim and P. Silberzan, Rep. Prog. Phys. **80**, 076601 (2017).
[8] X. Serra-Picamal, V. Conte, R. Vincent, E. Anon, D. T. Tambe, E. Bazellieres, J. P. Butler, J. J. Fredberg, and X. Trepat, Nat. Phys. **8**, 628 (2012).
[9] P. Rodríguez-Franco, A. Brugués, A. Marín-Llauradó, V. Conte, G. Solanas, E. Batlle, J. J. Fredberg, P. Roca-Cusachs, R. Sunyer, and X. Trepat, Nat. Mater. **16**, 1029 (2017).
[10] S. Tlili, E. Gauquelin, B. Li, O. Cardoso, B. Ladoux, H. Delanoë-Ayari, and F. Graner, R. Soc. Open Sci. **5**, 172421 (2018).
[11] X. Trepat, M. R. Wasserman, T. E. Angelini, E. Millet, D. A. Weitz, J. P. Butler, and J. J. Fredberg, Nat. Phys. **5**, 426 (2009).
[12] T. E. Angelini, E. Hannezo, X. Trepat, J. J. Fredberg, and D. A. Weitz, Phys. Rev. Lett. **104**, 168104 (2010).
[13] K. Doxzen, S. R. K. Vedula, M. C. Leong, H. Hirata, N. S. Gov, A. J. Kabla, B. Ladoux, and C. T. Lim, Integr. Biol. **5**, 1026 (2013).
[14] G. Duclos, M. Deforet, H. G. Yevick, O. Cochet-Escartin, F. Ascione, S. Moitrier, T. Sarkar, V. Yashunsky, I. Bonnet, A. Buguin *et al.*, in *Cell Migration* (Springer, New York, 2018), pp. 387–399.
[15] M. Deforet, V. Hakim, H. Yevick, G. Duclos, and P. Silberzan, Nat. Commun. **5**, 3747 (2014).
[16] J. Notbohm, S. Banerjee, K. J. Utuje, B. Gweon, H. Jang, Y. Park, J. Shin, J. P. Butler, J. J. Fredberg, and M. C. Marchetti, Biophys. J. **110**, 2729 (2016).
[17] D. Bi, X. Yang, M. C. Marchetti, and M. L. Manning, Phys. Rev. X **6**, 021011 (2016).
[18] D. L. Barton, S. Henkes, C. J. Weijer, and R. Sknepnek, PLoS Comput. Biol. **13**, e1005569 (2017).
[19] F. Giavazzi, M. Paoluzzi, M. Macchi, D. Bi, G. Scita, M. L. Manning, R. Cerbino, and M. C. Marchetti, Soft Matter **14**, 3471 (2018).
[20] T. Vignaud, H. Ennomani, and M. Théry, Methods Cell Biol. **120**, 93 (2014).
[21] See Supplemental Material at http://link.aps.org/supplemental/10.1103/PhysRevLett.122.168101 for experimental setup, image analysis and numerical simulations.
[22] J. W. Goodman, *Introduction to Fourier Optics* (Robertsand Company Publishers, 2005).
[23] L. Herve, O. Cioni, P. Blandin, F. Navarro, M. Men-neteau, T. Bordy, S. Morales, and C. Allier, Biomed. Opt. Express **9**, 5828 (2018).
[24] S. V. Kesavan, F. P. Navarro, M. Menneteau, F. Mittler, B. David-Watine, N. Dubrulle, S. L. Shorte, B. Chalmond, J.-M. Dinten, and C. P. Allier, J. Biomed. Opt. **19**, 036004 (2014).
[25] L. Petitjean, M. Reffay, E. Grasland-Mongrain, M. Poujade, B. Ladoux, A. Buguin, and P. Silberzan, Biophys. J. **98**, 1790 (2010).
[26] R. Farhadifar, J. C. Röper, B. Aigouy, S. Eaton, and F. Jülicher, Curr. Biol. **17**, 2095 (2007).
[27] D. Bi, J. H. Lopez, J. Schwarz, and M. L. Manning, Soft Matter **10**, 1885 (2014).
[28] S. Henkes, Y. Fily, and M. C. Marchetti, Phys. Rev. E **84**, 040301 (2011).
[29] A. Puliafito, L. Hufnagel, P. Neveu, S. Streichan, A. Sigal, D. K. Fygenson, and B. I. Shraiman, Proc. Natl. Acad. Sci. U.S.A. **109**, 739 (2012).
[30] C. Malinverno, S. Corallino, F. Giavazzi, M. Bergert, Q. Li, M. Leoni, A. Disanza, E. Frittoli, A. Oldani, E. Martini *et al.*, Nat. Mater. **16**, 587 (2017).